ACCSCIENCE PUBLISHING

International Journal of Bioprinting

RESEARCH ARTICLE

A novel method to enhance acoustic droplet bioprinting quality through the analysis of parametric influence mechanisms

Qing Guo, Siyu Li, Dachao Li[1]*, and Haixia Yu[2]*

State Key Laboratory of Precision Measurement Technology and Instruments, Tianjin University, Tianjin, China.

Abstract

Three-dimensional bioprinting ushers a transformative change in tissue engineering, providing unparalleled opportunities for regenerative medicine by precisely fabricating intricate, biomimetic tissues. To achieve true organ-level *in vitro* tissue construction, various advanced bioprinting technologies have been developed. Among these, acoustic droplet bioprinting technology, owing to its excellent biocompatibility and multi-sample handling capabilities, offers an efficient, non-contact liquid-handling approach for tissue engineering applications. To meet the printing structure's geometric precision requirements, meticulous control of printing parameters is essential. However, the selection of acoustic droplet printing parameters still depends heavily on empirical values, which often leads to print outcomes that fall short of optimal standards. In this paper, a parameterized droplet dispensing method for multi-sample droplet excitation was established. This method introduces a unified scaling parameter based on the product of surface tension and viscosity, integrating acoustic stress and fluid response into a single dimensionless quantity, thereby enabling precise adjustment of droplet velocity. The relative error between the initial velocity measured using this method and the preset velocity was less than 6.7%. Next, we analyzed the effects of droplet overlap distance and the Weber and Ohnesorge numbers on printed line-width consistency. By employing optimized printing parameters, we achieved controllable printing of patterned hydrogel meshes suitable for cell culture. The results demonstrated that the lengths and widths of the nine sub-meshes exhibited high consistency. These advances move acoustic droplet bioprinting from an experience-driven process toward a more systematic, predictive, and reproducible parameter-optimization strategy.

Keywords: Acoustic droplet bioprinting; Bioprinting parameters optimization; Parameterized droplet dispensing method

***Corresponding authors:**
Dachao Li
(dchli@tju.edu.cn)

Haixia Yu
(hxy2081@tju.edu.cn)

Citation: Guo Q, Li S, Li D, Yu H. A novel method to enhance acoustic droplet bioprinting quality through the analysis of parametric influence mechanisms. *Int J Bioprint*. 2026;12(1):622-636. doi: 10.36922/IJB025470490

Received: November 21, 2025
Revised: December 27, 2025
Accepted: December 31, 2025
Published online: January 8, 2026

1. Introduction

According to the latest statistics from the World Health Organization, nearly 2 million people worldwide require organ transplantation each year, whereas organ availability remains far below demand (supply–demand ratio < 1:20).[1] Organ shortages present the biggest challenge for organ transplant recipients. In recent years, the rapid advancement in

tissue engineering has shown great potential in addressing the "organ transplant crisis."[2] Tissue engineering, an emerging science developed in the late 1980s, involves the interdisciplinary fusion of clinical medicine, biomaterials, cell biology, bioengineering, and other fields.[3] It aims to establish three-dimensional (3D) complexes of cells and biomaterials using bioactive substances through *in vitro* cultivation or construction methods to replace or repair damaged organs.[4]

To achieve true organ-level *in vitro* tissue construction, researchers have developed various advanced 3D bioprinting technologies, including extrusion-based bioprinting,[5,6] inkjet bioprinting,[7,8] laser-assisted bioprinting,[9,10] and stereolithography bioprinting.[11,12] These technologies, characterized by high printing resolution, rapid fabrication speed, and advanced automation, are pivotal to the evolution of tissue engineering.[13] However, nozzle-dependent bioprinting methods, such as extrusion-based and inkjet bioprinting, typically face the following challenges: (i) High concentrations and viscosities of bioinks can lead to nozzle clogging, thereby reducing droplet distribution accuracy[14]; and (ii) the transient high pressure and shear forces generated at the nozzle during the distribution of biomolecules and cells can damage bioactive materials.[15,16] Conversely, while nozzles do not constrain laser-assisted and stereolithographic printing methods, residual reagents can readily cause biological materials to lose activity.[17]

Compared with other 3D bioprinting techniques, acoustic droplet bioprinting employs focused ultrasound to dispense bioinks in a non-contact manner with high spatial precision and without nozzle-induced constraints.[18] The absence of physical contact and shear-inducing nozzles minimizes mechanical stress on cells and biomaterials, thereby preserving bioactivity and viability. In addition, its capability to handle diverse bioinks without clogging enables flexible, multi-material deposition, which is particularly advantageous for constructing complex tissue and organ-like architectures.[19] Owing to these features, acoustic droplet bioprinting offers distinct advantages for tissue and organ printing and has attracted increasing attention in the field.

In 2021, Jentsch *et al.*[20] successfully fabricated complex 3D hydrogel structures laden with cells using acoustic droplet bioprinting technology, without adversely affecting the proliferation or differentiation capacity of stem cells. Xia *et al.*,[21] Chen *et al.*,[22] and Gong *et al.*[23] integrated personalized medicine with acoustic droplet bioprinting to construct reliable tumor models. These models not only closely mimic the *in vivo* tumor microenvironment but also enable objective and accurate assessment of drug efficacy and safety. However, the lack of precise optimization in the dynamic control of acoustic droplet bioprinting parameters results in poor consistency in multi-sample droplet ejection and challenges in achieving the desired structural precision of *in vitro* tissue models.[23]

Current studies on control methods rely predominantly on empirical observations. For example, Jentsch *et al.*[19] reported that the droplet impact velocity varies linearly with ultrasonic electrical input power, while the droplet diameter is inversely proportional to the ultrasonic frequency. In addition, Fang *et al.*[24] experimentally demonstrated that the droplet diameter increases with increasing pulse duration. Although these findings provide useful insights into the controllable dispensing of droplets in acoustic droplet bioprinting, they do not offer a systematic analysis of how the complex fluid properties of bioinks influence droplet generation and key characteristic parameters.

The commonly used input power control methods for acoustic droplet bioprinting include power scanning and dynamic fluid analysis methods. The method of power scanning involves a step-by-step incrementation of the acoustic energy until the ideal droplet initial velocity is obtained. Although implementation is straightforward, the process requires a substantial time investment.[24,25] In 2016, Hadimioglu *et al.*[18] developed a dynamic fluid analysis technique, which evaluates threshold power by analyzing the dynamic response of the liquid surface under focused acoustic energy. This method enables the automated assessment of the minimum input power needed for droplet excitation, but identifying the specific input power that matches the desired droplet initial velocities is difficult. The aforementioned studies fail to provide a viable solution for the controllable dispensing of multiple samples.

On the other hand, apart from ensuring stable droplet ejection, analyzing the impact of printing parameters on print quality, such as line width and its smoothness, is crucial for high-fidelity *in vitro* tissue construction. Gudapati *et al.*[26] emphasized in their review that the spreading characteristics of bioink droplets on the substrate significantly impact printing resolution and structural integrity. Gong *et al.*,[27] in their optimization study of linear bioprinting processes, found that droplet spreading characteristics are influenced by multiple factors, including substrate wettability, collision velocity, and droplet volume. Current research still lacks a correlation analysis of the impact of printing parameters on print quality. Relying solely on empirical methods makes it challenging to achieve high-precision and reproducible printing of *in vitro* tissue models.

Therefore, our method first introduces a unified scaling parameter based on the product of surface tension and viscosity, integrating acoustic stress and fluid response

into a single dimensionless quantity. By analyzing the correlations among input power, droplet velocity, and this liquid-property product, the input power required to excite droplets to a target velocity can be accurately predicted for bioinks with known properties. This capability enables controlled bioprinting of diverse bioinks, significantly reducing the reliance on extensive power scanning, thereby shortening experimental time and improving reproducibility.

Next, a direct correlation between input power and line width was established by analyzing the effects of input power and droplet characteristic parameters, as well as the influence of the droplet overlap distance, Weber number (*We*), and Ohnesorge number (*Oh*) on line width. To verify the feasibility, patterned hydrogel meshes for cell culture were printed. By integrating the predictive velocity control and optimized printing parameters, we demonstrated the fabrication of hydrogel mesh structures with high dimensional consistency. The lengths and widths of the nine subgrids exhibited excellent consistency.

2. Materials and methods

2.1. Experimental system

The acoustic droplet bioprinting system consists of four components: a liquid-depth measuring system, a droplet-excited system, a high-speed visualization system, and a target substrate (Figure 1). The liquid depth measuring system consists of an oscilloscope (DS7000, Rigol, China) and a pulser/receiver (5072PR, Olympus, Japan). They were utilized to measure the depth of the liquid within the wells and to align the transducer focal point onto the liquid surface. The droplet-excited system includes a power amplifier (75A250, Amplifier Research, USA), a 5-MHz-focused ultrasound transducer (V309S-SU, Olympus, Japan), and an arbitrary waveform generator (DG5000, Rigol, China), which were utilized for generating the required acoustic energy. The ultrasound transducer has an active aperture diameter of 12.7 mm and a focal length of 19.43 mm, corresponding to an f-number of 1.53. The focal zone was characterized by an axial length of 5.24 mm and a lateral diameter of 0.47 mm. The high-speed visualization setup (SA-X2, Photron, Japan) was used to record the entire process of droplet excitation, upward flight, and printing onto the target substrate at 12,500 fps.

Droplet diameter and velocity were measured using contour detection and centroid-extraction algorithms. During the experiments, 48-well plates (each well with a diameter of 11.5 mm and a depth of 17 mm) served as the source liquid wells, while glass slides measuring 26 × 76 mm with a thickness of 1 mm acted as the target substrate. The glass slide was positioned 0.50 cm above the liquid surface.

2.2. Reagents and materials

Gelatin methacrylate (GelMA) solutions (≥98% purity; Psaitong, China) at various concentrations, containing 10 μm polystyrene green fluorescent microspheres (G1000B, ThermoFisher, USA), were used as the experimental media (Table 1). GelMA is commonly used as a bioink due to its adjustable physicochemical properties, excellent biocompatibility, and close resemblance to natural extracellular matrices.[28,29] Polystyrene microspheres with sizes, shapes, and surface properties approximating those of cells were chosen as cell surrogates to simplify analysis.[19]

Because GelMA solutions are thermosensitive, viscosity decreases at 37°C, improving flowability and printability.

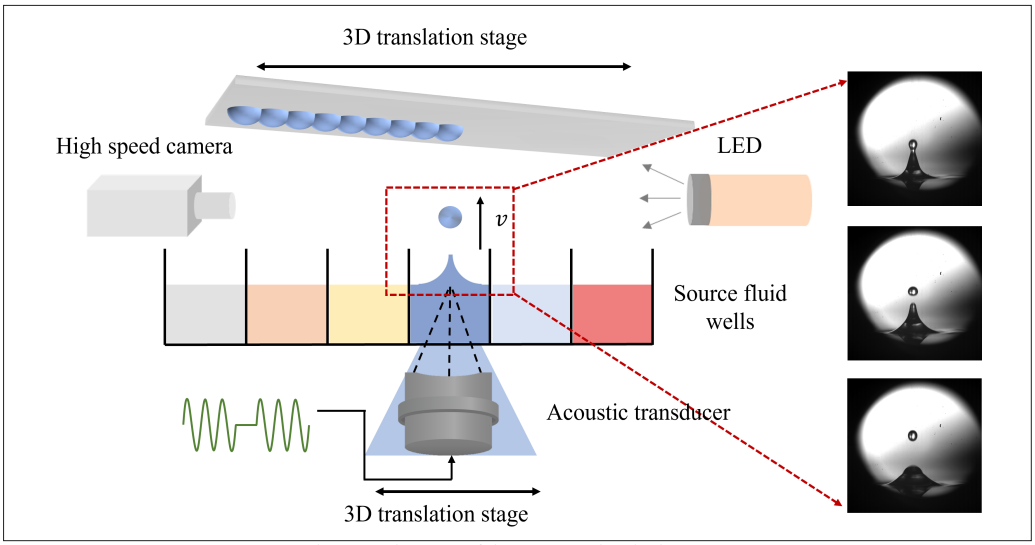

Figure 1. Schematic diagram of the acoustic droplet bioprinting system.

This characteristic makes GelMA hydrogel more suitable for bioprinting. Therefore, during the experimental process, a temperature control system (ED330, Jiangsu Huakai Electric Heating Appliances Co., Ltd., China) was utilized to heat the source fluid wells. The temperature control system consists of a polyimide heating film, an intelligent digital temperature controller, and a power adapter. The temperature control system achieves a precision of 0.1°C, with a temperature deviation not exceeding 0.5°C.

To develop a parameterized droplet dispensing method, it is crucial to measure the liquid properties in advance. The surface tension of bioink was measured by a surface tension instrument (CV-ZL1020, CVOK, China). The viscosity was measured by an automatic digital viscometer (DV3TLV, Brookfield, USA). Each value represents the mean of six measurements. During the measurements, a small heating plate was placed beneath the glass container holding the test reagent, maintaining the liquid temperature at 37°C. According to the measurements, the GelMA-based inks containing 10 or 20 μm polystyrene microspheres exhibited viscosities in the range of 8.36–10.91 cP and surface tensions between 36.82 and 50.52 mN/m. In addition, to ensure the uniform distribution of microspheres in the GelMA solution, both the printing and liquid properties measurement experiments were conducted within 10 min after stirring.

2.3. Statistical analysis

All quantitative data are expressed as mean ± standard deviation (SD). Each experimental condition was independently repeated at least five times ($n \geq 5$), as specified in the corresponding figure captions. Correlation analyses between printing parameters (e.g., acoustic input power, droplet overlap distance, *We*, and *Oh*) and printing outcomes (e.g., droplet velocity and printed line width) were performed using linear regression analysis. The goodness-of-fit was evaluated by the coefficient of determination (R^2). For comparisons involving variability in printed line width, the coefficient of variation (CV) was used as the primary quantitative metric to assess printing consistency. CV was calculated as the ratio of the SD to the mean value of the measured line width. Statistical analyses and data fitting were performed using Origin (version 2021, OriginLab Corporation, USA). Image analysis and quantitative measurements were conducted using ImageJ (version 1.53, National Institutes of Health, USA).

3. Results and discussion

3.1. Parameterized droplet dispensing method

Previous studies have shown that with increasing input power, the droplet diameter varies minimally, while the initial velocity is easily detectable and linearly increases.[18] Subsequent droplet excitation experiments were conducted on the reagents listed in Table 1, aiming to establish quantitative correlations between liquid properties (e.g., viscosity and surface tension), input power, and droplet initial velocity. Given the propensity of droplets to exhibit unstable excitation at lower input power and the potential for secondary droplet formation at excessively high input power, the input power control range needs to be defined within an interval extending from the threshold power, corresponding to the point of zero initial velocity, to the maximum power point, where the onset of secondary droplet formation occurs.

As shown in Figure 2, the linear correlation between velocity and input power was significantly influenced by the liquid properties. With the increase in microsphere concentration in the GelMA solution, the slope also varied. The linear correlations between droplet initial velocity and input power for the six reagents from A to F were as follows: $y = 0.57176x - 1.15969$ ($R^2 = 0.97$), $y = 0.38632x - 0.65024$ ($R^2 = 0.98$), $y = 0.34184x - 0.52587$ ($R^2 = 0.99$), $y = 0.32956x - 0.49615$ ($R^2 = 0.98$), $y = 0.29551x - 0.48313$ ($R^2 = 0.99$), and $y = 0.27658x - 0.44181$ ($R^2 = 0.99$).

This pattern can be attributed to the addition of microspheres, which results in a change in the liquid properties. The differences were primarily reflected in

Table 1. Characteristics of the experimental fluids

Liquid name	Density (g/cm^3)	Surface tension (mN/m)	Dynamic viscosity (cP)	Speed of sound (m/s)
A	1.03	36.82	8.36	1526
B	1.02	45.52	9.44	1523
C	1.01	46.11	9.52	1515
D	1.00	47.23	9.58	1497
E	0.98	49.88	10.12	1490
F	0.94	50.52	10.91	1526

Notes: A: 5% gelatin methacrylate (GelMA), B: 5% GelMA with 1.81×10^5 microspheres/mL, C: 5% GelMA with $5 \times 1.81 \times 10^5$ microspheres/mL, D: 5% GelMA with 1.81×10^6 microspheres/mL, E: 5% GelMA with $5 \times 1.81 \times 10^6$ microspheres/mL, F: 5% GelMA with 1.81×10^7 microspheres/mL.

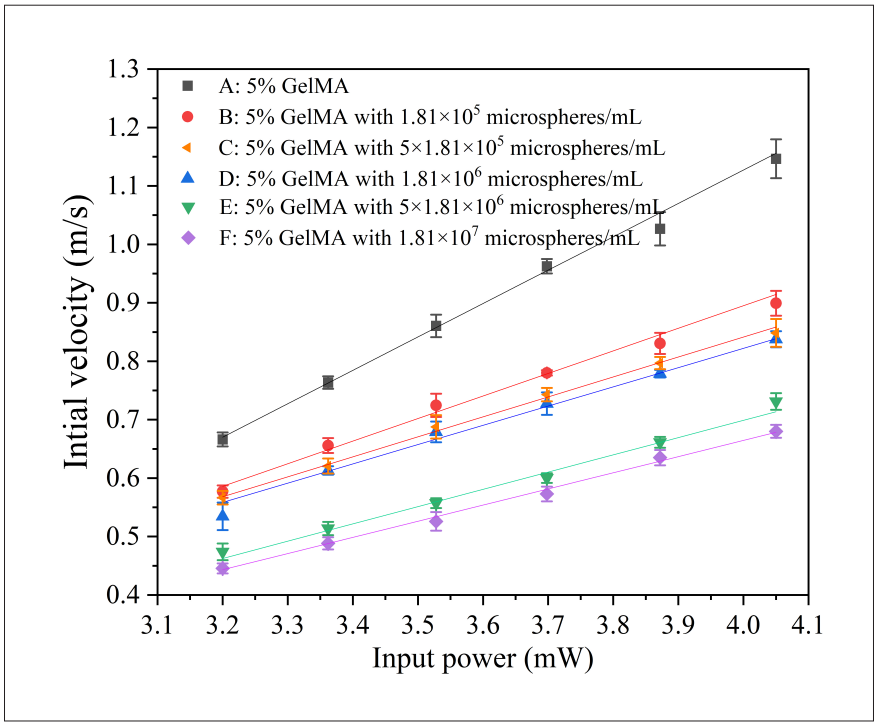

Figure 2. Correlation between droplet initial velocity and input power. Each experimental data point was obtained by averaging five repeated measurements. Abbreviation: GelMA, gelatin methacrylate.

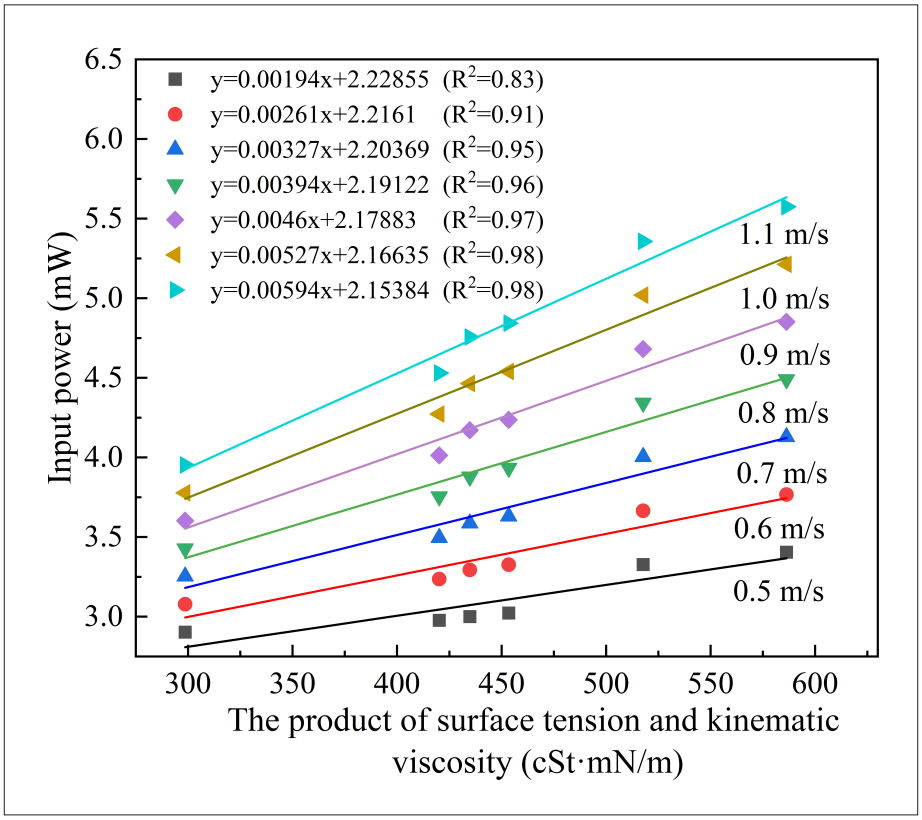

Figure 3. Correlation between input power and the product $\sigma\nu$ at specific initial velocities.

density, surface tension, and viscosity. Therefore, we introduced the product of surface tension σ and kinematic viscosity ν[30,31] and developed a parameterized droplet dispensing method by establishing the correlation between droplet initial velocity, input power, and the product $\sigma\nu$. The fluid's kinematic viscosity ν was calculated by dividing its dynamic viscosity by the fluid's density.

As the concentration of microspheres increases, the products $\sigma\nu$ of these reagents from A to F were determined to be 298.61, 420.15, 434.82, 453.41, 517.75, and 586.30 cSt·mN/m. With the increase in $\sigma\nu$, the internal resistance to flow and intermolecular forces also increase. This requires higher input power to achieve the target velocity. Therefore, for bioinks exhibiting a greater $\sigma\nu$, the slope of the linear fitting equation was smaller.

To examine the correlation between the $\sigma\nu$, velocity, and input power, we extracted input power data for initial droplet velocities (0.5–1.1 m/s) from Figure 2 and conducted a linear fit, as shown in Figure 3. Establishing this correlation is essential for developing the parameterized droplet dispensing method during acoustic droplet bioprinting. Based on these linear correlations, we predicted the input power corresponding to seven specific velocities by measuring the liquid properties of bioinks in advance. Furthermore, by refitting the linear correlations using seven velocity points and their corresponding predicted input powers, the input power for other velocities (0–1.1 m/s) can be determined under the given experimental system.

3.2. Verification of parameterized droplet dispensing method

To verify the accuracy of the parameterized droplet dispensing method, three test reagents were used: G (5% GelMA with 1.12×10^6 microspheres [20 μm]/mL), H (7.5% GelMA with 1.81×10^5 microspheres [10 μm]/mL), and I (7.5% GelMA with 1.81×10^7 microspheres [10 μm]/mL). The $\sigma\nu$ of the three reagents were measured as 303.51, 697.82, and 934.23 cSt·mN/m, respectively. Incorporating these liquid properties into the linear correlations shown in Figure 3, the required input power for specific initial velocities could be calculated. Using the calculated input power to eject droplets, the resulting initial droplet velocities closely matched the preset values, as shown by the black square in Figure 4.

To evaluate the predictive accuracy of the required input power at other velocities, droplet excitation experiments were conducted by randomly selecting six sets of input power. As shown by the blue square in Figure 4, the experimentally obtained average droplet initial velocities coincide perfectly with the preset values based on the linear fitting equation. The maximum relative error of velocities remained below 6.7%. This error primarily arises from inaccuracies in measuring surface tension and viscosity, temperature control deviations, and systematic errors.

3.3. Effect of droplet overlap distance on line width

For a bioprinted object, discrete droplets must be placed at a specific overlap distance to form a continuous line, which is then stacked to construct a patterned structure.[32] To ensure consistent bioprinting outcomes, we kept all other variables constant and specifically analyzed the influence of droplet overlap distance L on bioprinting quality after achieving controllable dispensing of multiple bioink droplets. L is defined as the center-to-center spacing of the droplets, or the step length of the stage movement. The bioprinting quality was evaluated by analyzing the CV of the line width. The steps for extracting line width and its CV are detailed below:

(i) A CCD camera (Model 1600, PCO AG, Germany) was installed on an inverted fluorescence microscope (Axio Observer A1, Zeiss, Germany) to capture fluorescent images of the printed structures following ultraviolet (UV) curing.

(ii) Image processing algorithms were applied to outline the edge contours of the fluorescent images, identifying the center points.

(iii) The center point was designated as the origin, and all line width values within the x-coordinate range of $-L/2 \times (n-1)$ to $L/2 \times (n-1)$ were extracted through 100 sampling points, where n represents the number of printed droplets.

(iv) Their mean and SD were computed, and the CV of the line widths was used as the final evaluation metric.

The experimental medium used for droplet printing was 5% GelMA with 1.81×10^6 microspheres (10 μm)/mL. The input power was set to 3.33 mW, resulting in an initial droplet velocity of 0.60 m/s and a droplet diameter of 385 μm. The spreading diameter D_s of the droplet onto the substrate surface was 660 μm.

To analyze the effect of L on line width, it is necessary to achieve coordinated control between the droplet-excited setup and the displacement platform. The displacement platform was purchased from Zolix Instruments Co., Ltd. (uKSA 100). It has a travel range of 100 μm along the x-axis and 50 μm along the y-axis, with a repeatability positioning accuracy of ±2 μm. While the transducer remained stationary, the substrate was translated along the x-axis at a speed of 10 mm/s with a delay time of 0.5 s and a motion of L mm. When the program was started, the transducer was

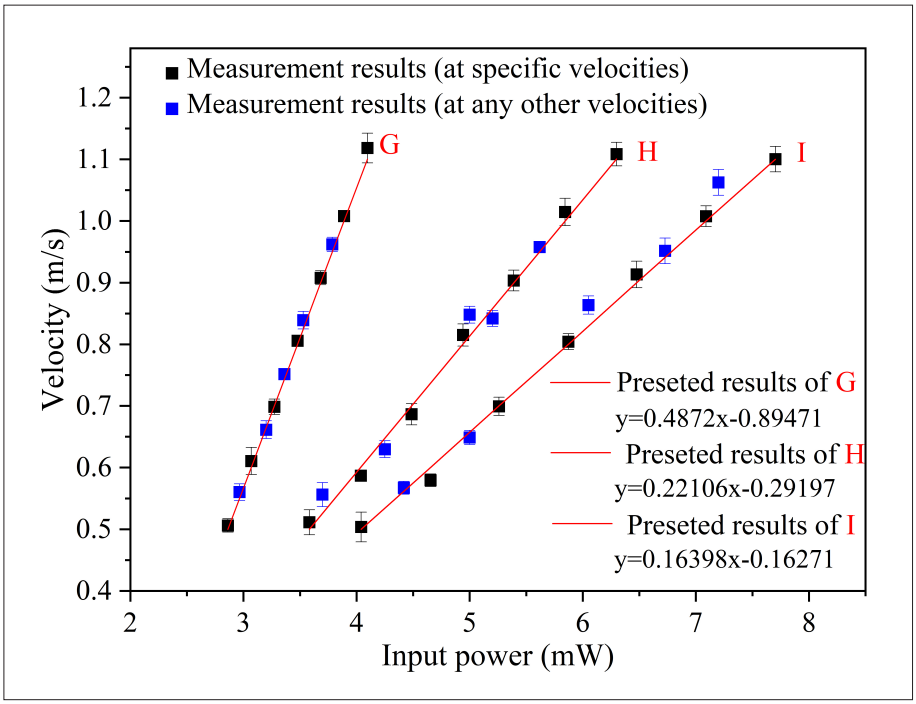

Figure 4. Correlation between input power and the product σv at specific initial velocities. Each experimental data point was obtained by averaging five repeated measurements.

triggered, with a time interval of 0.558 s between single pulses. Once the target substrate was positioned within 0.5 s based on the specific L, the second droplet collided and coalesced with the already printed one.

During the droplet collision, the surface tension promotes coalescence, and the viscosity resists shearing motion.[33,34] When the overlap distance L is small, the droplets have a larger contact area. Due to the initial kinetic energy of the upward flying droplets, the axial momentum during droplet collision is converted into radial momentum, causing the coalesced droplets to undergo expansion and enlargement along the center point. Under these printing conditions, the average line width will be relatively larger. As the L increases, the contact area between droplets decreases, leading to a more uniform distribution of material in the junction area and thereby smoothing the boundaries. When the L continues to increase, the connection gradually becomes concave, assuming a wavy shape, and the average line width decreases. The blue fluorescence images in Figure 5 show printing outcomes at different overlap distances.

As shown in Figure 5A, when the overlap distance was 0.50 mm ≤ L ≤ 0.66 mm, the line boundaries were smooth, and the SD of the line width was minimized, with all CVs being less than 1%. Binary-droplet printing is a building block for forming continuous lines. During multi-droplet printing, collisions and coalescence among droplets occur more frequently. The increased complexity of internal fluid dynamics in this process requires more precise control over the overlap distances between droplets to achieve smooth boundaries. To assess the suitability of the selected range of overlap distances for multi-droplet printing, we conducted continuous printing experiments using 5 and 10 droplets.

For the continuous printing of five droplets, the CV of the line width was less than 1% only within the overlap distance of 0.50 mm ≤ L ≤ 0.60 mm. In addition, it was verified that this overlap distance also applies to the continuous printing of 10 droplets, with no further reduction in the corresponding range (Figure 5B). Therefore, for multi-droplet printing, the range of 0.56–0.60 mm is considered the optimal selection. The optimal L results from the interplay of droplet size, impact velocity, liquid properties, and substrate wettability, which collectively regulate the balance between inertial spreading, capillary coalescence, and viscous dissipation under the present experimental conditions.

To extend printing parameters to a broader range of reagent compatibility, this study introduced the collision parameter P to normalize the collision overlap distance, enhancing parameter adaptability. P is given by the ratio L/D_s. The optimal overlap distance is 0.56–0.60 mm, corresponding to a collision parameter range of

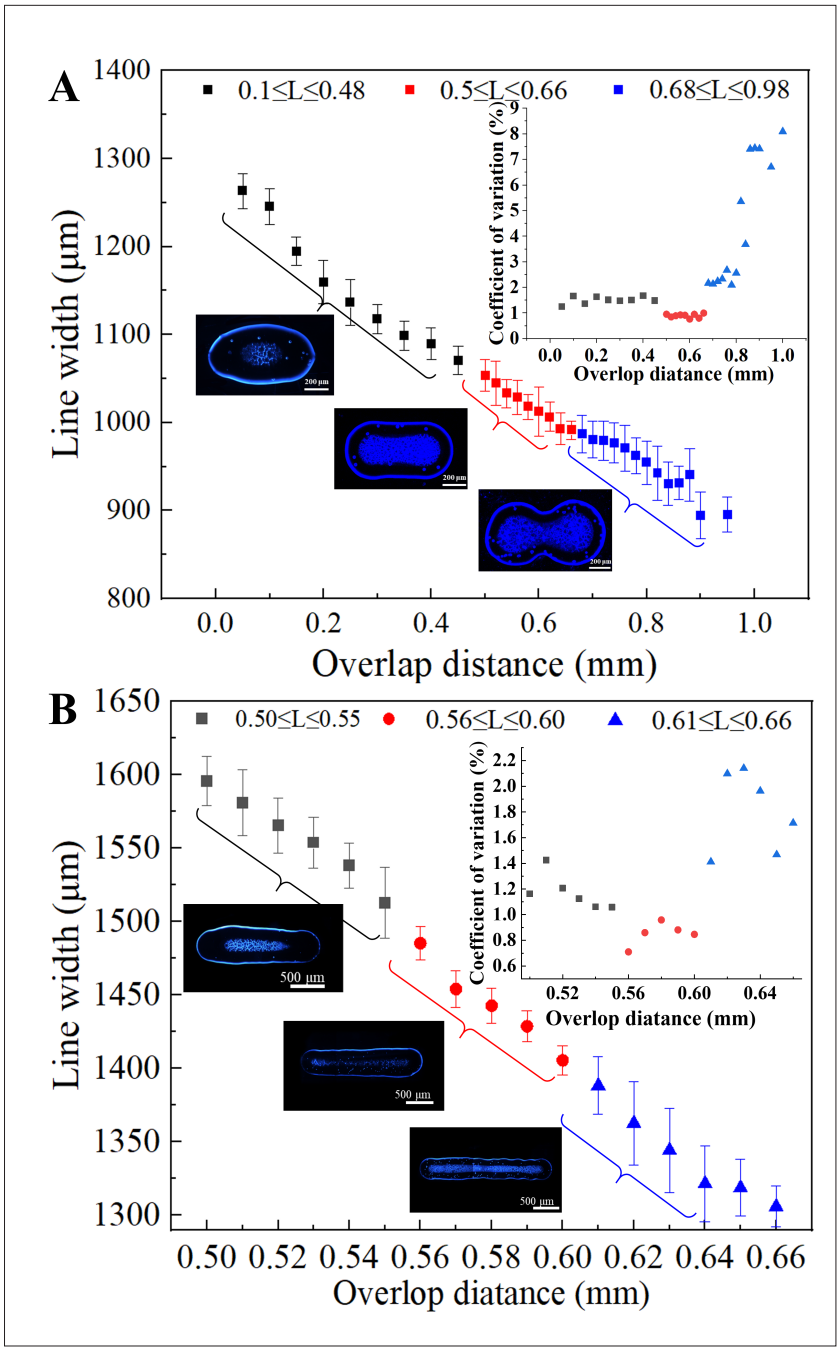

Figure 5. Correlation between droplet overlap distance and line width for (A) five-droplet and (B) 10-droplet printing. The inset graphs represent the coefficients of variation of line width under different droplet overlap distances. The inset blue fluorescent images indicate the printing effect under different droplet overlap distances (scale bars: [A] 200 μm, [B] 500 μm; magnifications: [A] 5×, [B] 5×). Each experimental data point was obtained by averaging five repeated measurements.

Table 2. Printing results of different bioinks

Reagent	Spreading diameter *Ds* (μm)	Collision parameter *P*	Average line width (μm)	Standard deviation	Coefficient of variation (%)
B	678	0.86	1462.35	9.87	0.67
F	634	0.88	1446.83	10.12	0.70

$0.85 \leq P \leq 0.91$. Next, the 10-droplet continuous printing experiment was conducted using reagents B and F to validate the applicability of the optimal L across different bioinks. Using the parameterized droplet dispensing method, the input power required to reach an initial velocity of 0.60 m/s was first determined as 3.24 and 3.77 mW for reagents B and F, respectively.

As shown in Table 2, the spreading diameters of the two bioinks, B and F, were 678 and 634 μm, respectively. Within the range of $0.85 \leq P \leq 0.91$, a set of parameters was selected for the 10-droplet continuous printing experiment. The results demonstrate that the line width's CV for both bioinks remained within 1%. Thus, the collision parameter range determined in this study not only accommodates various bioinks but also aids researchers in achieving smooth line printing more rapidly.

3.4. Effect of droplet characteristic parameters on bioprinting quality

In the process of 3D bioprinting, the characteristic parameters of droplets, such as velocity and volume, are also crucial to the interactions at the collision interface and the formation of the desired final pattern. The *We* is dimensionless, calculated as the ratio of inertial force to surface tension force. Using the *We*, we can normalize the effects of droplet velocity and volume, allowing for a more direct comparison of different printing conditions and the resulting print quality.

$$We = \frac{2\rho v^2 R_0}{\sigma} \quad (1)$$

where v and R_0 are the collision velocity and radius of the flying droplet, respectively, and ρ and σ are the density and surface tension of the droplets, respectively. The collision velocity of the droplet can be automatically extracted according to its initial velocity and flight height (0.5 cm). According to the experimental results in **Section 3.3**, as the droplet number increased to 10 or more, the resulting line width stabilized, showing no significant increase. Therefore, the subsequent analysis was confined to the line width resulting from the printing of 10 droplets. Under the $0.85 \leq P \leq 0.91$v, the experiment achieved droplet printing under varying collision *We*s by adjusting the input power. According to previous experimental results, it was found that higher input power leads to increased droplet ejection and collision velocities, and decreased droplet volume.

As shown in Figure 6A, for continuous 10-droplet printing, the line width decreased linearly as the *We* increased. This is mainly attributed to the reduction in droplet volume and its spreading diameter. The line widths' CVs were less than 1% for the three overlap distances. The results indicate that the collision parameter range established in **Section 3.3** is equally applicable under varying *We*s. On the other hand, according to the linear equation in Figure 6, it is possible to achieve controllable printing of specific line widths within the *We* range of stable droplet excitation.

However, when reagents were changed or ultrasonic transducers with different frequencies were used, resulting in variations in droplet size, achieving consistent printing of specific line widths becomes challenging. This is because the *We* exhibits low sensitivity to changes in droplet diameter and does not account for viscosity effects.

The *Oh* integrates viscosity, surface tension, and droplet size, offering a more comprehensive view of the droplet's resistance to deformation and spreading. The subsequent analysis was focused on the impact of the *Oh* on line width.

$$Oh = \frac{\mu}{\sqrt{2\rho\sigma R_0}} \quad (2)$$

Figure 7 shows a strong linear correlation between the *Oh* and line width.

By analyzing the effects of input power and droplet characteristic parameters in **Section 3.2**, as well as the influence of the *L*, *We*, and *Oh* numbers on line width, a direct correlation between input power and line width can be established. However, the current method for predicting line width is limited to a single reagent. To extend this method to other reagents, a preliminary 10-droplet printing experiment should first be conducted at a fixed *L* to establish the corresponding relationships between the *We*, *Oh*, and line width. Based on these correlations and the parameterized droplet dispensing method, printing with a targeted line width can then be achieved predictably.

3.5. Patterned hydrogel mesh printing

In this section, we leveraged the optimal parameter combination established in previous research to print a patterned hydrogel mesh structure designed for cell culture, thereby validating the effectiveness of the previously proposed printing control strategy.

The mesh structure mimics a basic scaffold, offering a porous framework that resembles the extracellular matrix in tissues.[35] This allows researchers to verify whether the printed structure can provide sufficient mechanical support and a suitable environment for cell adhesion and growth, key prerequisites for tissue engineering applications. The mesh, typically a simple crisscross pattern of intersecting

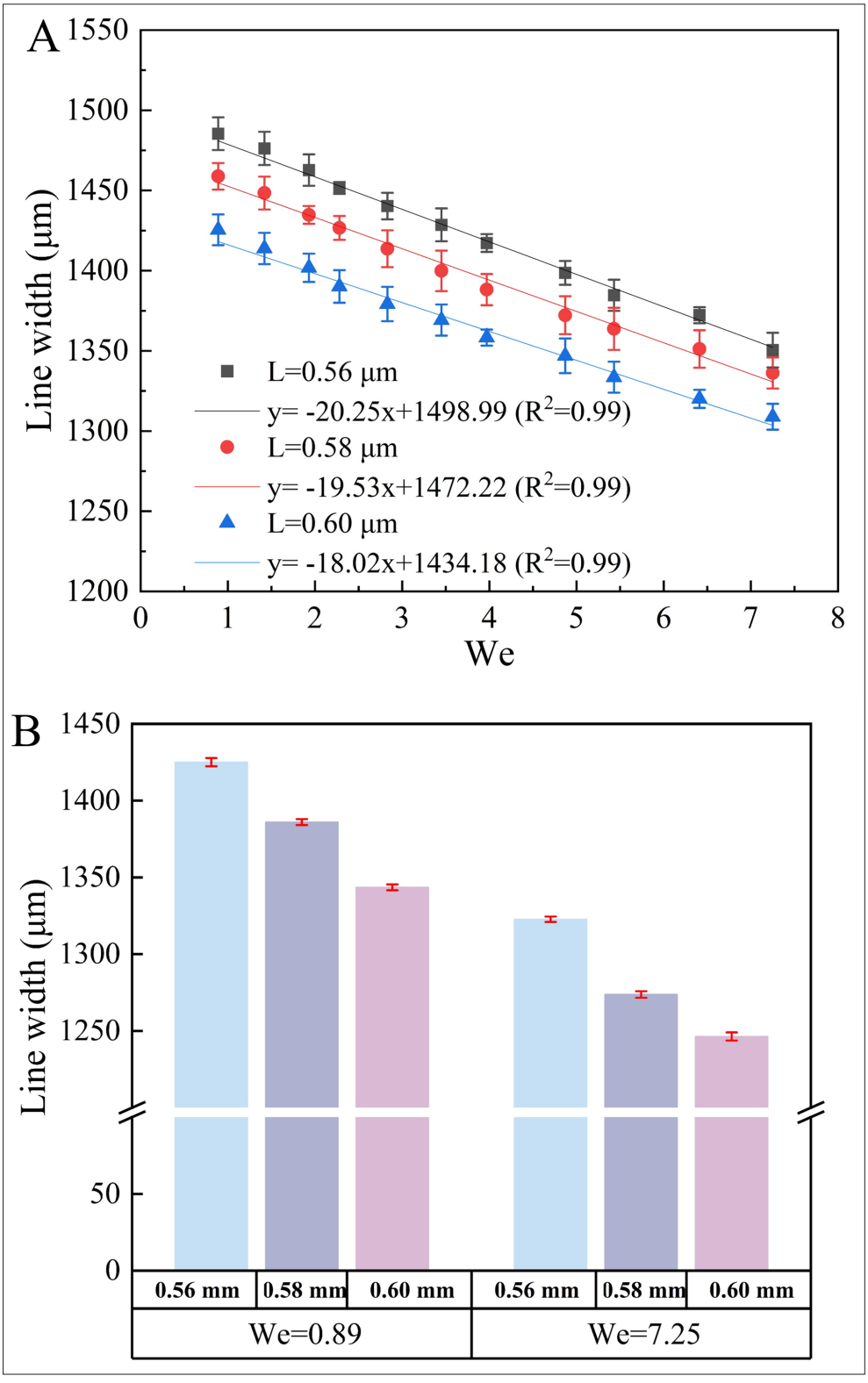

Figure 6. Quantitative evaluation of the influence of Weber number (*We*) on printing performance and stability. (A) Correlation between line width and *We*. (B) Repetitive experiments for the maximum and minimum *We* at the optimal droplet overlap distance. Each experimental data point was obtained by averaging five repeated measurements.

lines, along with evenly spaced horizontal and vertical lines, provides a clear benchmark for measuring line width, consistency of spacing, and dimensional accuracy.

The experimental medium was 5% GelMA (with photoinitiator) mixed with 1.81×10^6 polystyrene microspheres (10 μm)/mL, printed using acoustic excitation at 4.05 mW, with an L of 0.60 mm. As shown in Figure 8A, the first printing path involved depositing four lines, along the x-axis, with a center-to-center spacing d_1 of 2.5 mm. After printing, the first layer was UV-cured (5–10 s) to restrict liquid flow. Subsequently, the displacement platform was repositioned to the lower-left corner, and four lines were printed in the same manner along the y-axis with a center-to-center spacing d_2 of 2.5 mm, constituting the second layer.

The printed result shown in Figure 8B revealed that the first layer exhibited uniform and smooth lines, yet the second layer showed ink droplet aggregation, resulting in uneven line width. This phenomenon is mainly caused by ink droplets contacting both the hydrophobic cured first layer and the hydrophilic substrate during the second-layer printing process. The difference in wettability at the interface hinders normal droplet spreading at the junction, thus affecting the uniformity and smoothness of the second layer. An image processing approach was employed to detect the contours of each sub-mesh and fit minimum bounding rectangles, enabling the identification and measurement of the width and height of each sub-mesh. The results revealed that the lengths and widths of the nine sub-meshes exhibited poor consistency.

To improve the uniformity of the second layer, the printing path was optimized by implementing an intermittent printing approach. The initial printing position was redefined by setting a point 0.60 mm above the original y-axis coordinates as the starting point for the second-layer printing, followed by the continuous deposition of three droplets with a droplet overlap distance L' of 0.60 mm At an input power of 4.05 mW, employing the control method described in **Section 3.3**, the droplet initial velocity and collision velocity were calculated as 0.87 and 0.78 m/s, respectively, with a measured droplet diameter of 377.25 μm. Therefore, with a We of 4.87, the theoretical line width was determined to be 1346.42 μm based on the formula presented in Figure 6A.

When the d_1 was 2.5 mm, the dimensions of a single sub-mesh were 1.15 × 1.15 mm. Given that $L' < 1.15$ mm $< 2L'$, the consecutive printing of three droplets can ensure the formation of side walls of the sub-mesh.

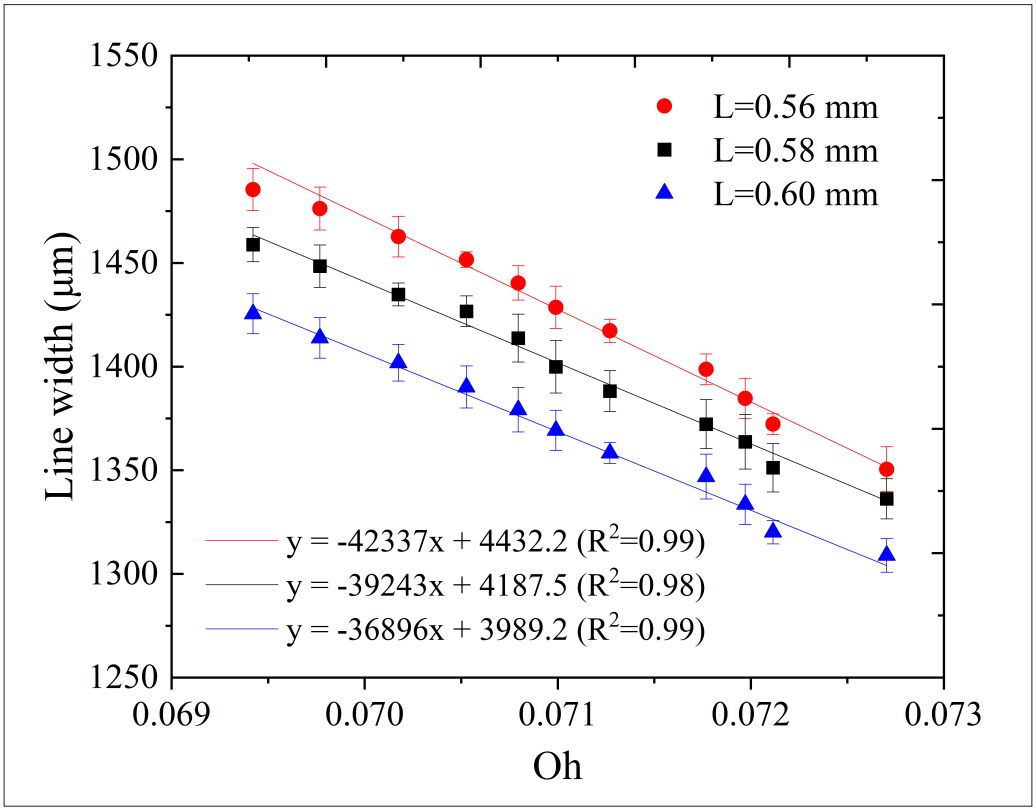

Figure 7. Correlation between line width and Ohnesorge number. Each experimental data point was obtained by averaging five repeated measurements.

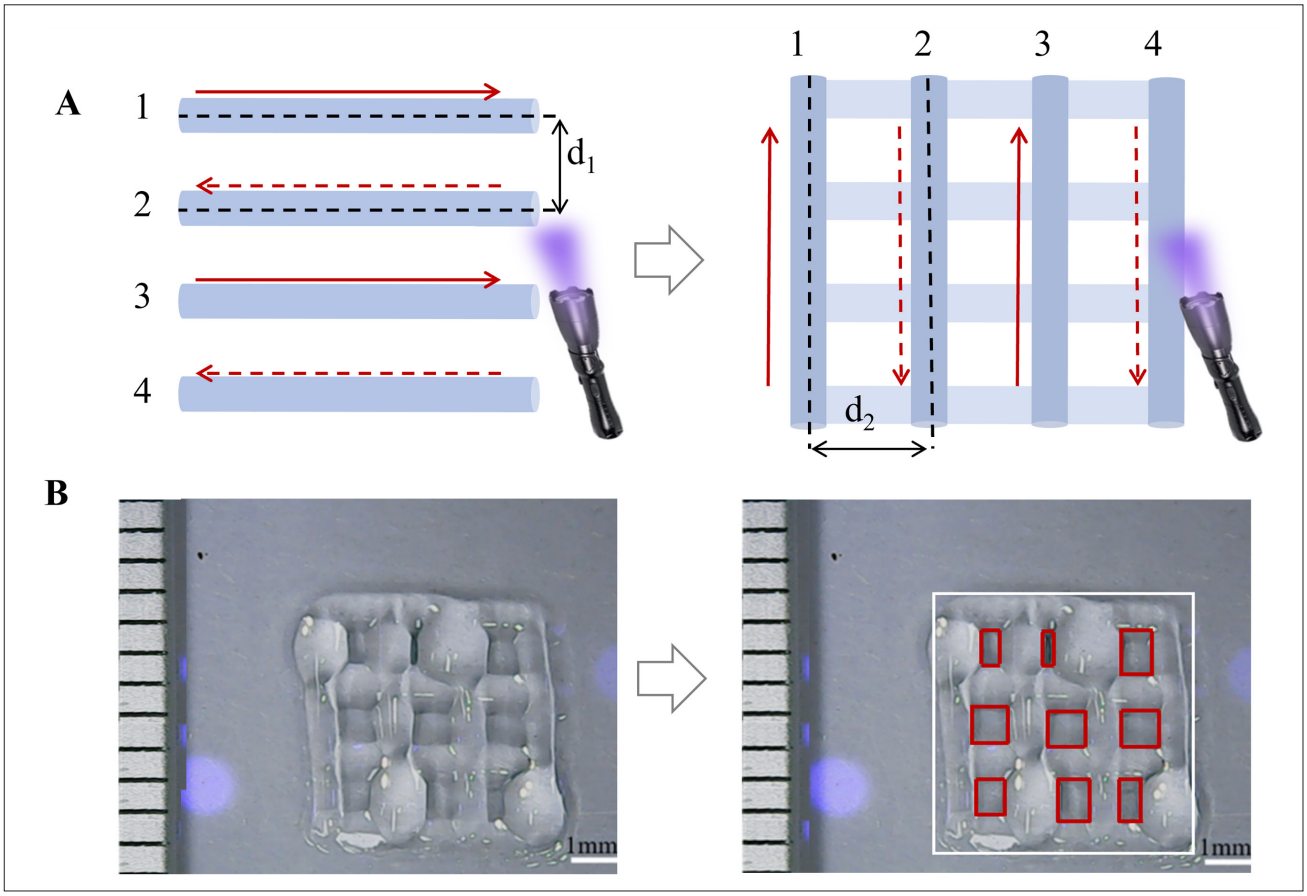

Figure 8. Schematic of the printing path for (A) the mesh scaffold structure and (B) photographs of the printed object.

Building on this foundation, by moving 2.5 mm along the *x*- and *y*-axes and sequentially printing the other eight sidewalls, the complete structure can be achieved. Following scheme optimization, the second-layer printing performance surpasses the results depicted in Figure 8B, exhibiting enhanced uniformity and smoothness in the overall structure, alongside a significant improvement in the consistency of mesh specifications (Figure 9). Next, five repeated printing experiments of the mesh structure were conducted, and the length and width of nine sub-meshes were extracted from each of the five experimental groups. Comparative analysis results revealed that the CV for both length and width in each group did not exceed 3%, with the relative error between measured and preset dimensions across all groups remaining below 6% (Table 3).

4. Conclusion

This study focused on addressing two fundamental challenges in acoustic droplet bioprinting: (i) poor consistency during multiple droplet generation, and (ii) low fidelity of printed structures under multi-parameter influences. To achieve controllable droplet excitation and obtain uniform linear structures, we first conducted experimental investigations to explore the correlation between the initial velocity of droplets and acoustic input power. By introducing a unified scaling parameter based on the product of surface tension and viscosity, a parameterized droplet dispensing method was established, allowing the prediction of the acoustic input power required to achieve specified droplet velocities for GelMA-based bioinks under the given acoustic configuration. The experimental validation results revealed that the relative errors between target droplet velocities and measured velocities using the selected excitation power, and the measured velocities were consistently less than 6.7%. Although this control strategy is not directly transferable to other acoustic systems without recalibration, the underlying theoretical scaling framework is general and can serve as a quantitative reference for efficient excitation parameter determination in future acoustic droplet printing studies.

Next, this study conducted a thorough analysis of the effects of droplet overlap distance (L), We, and Oh on line

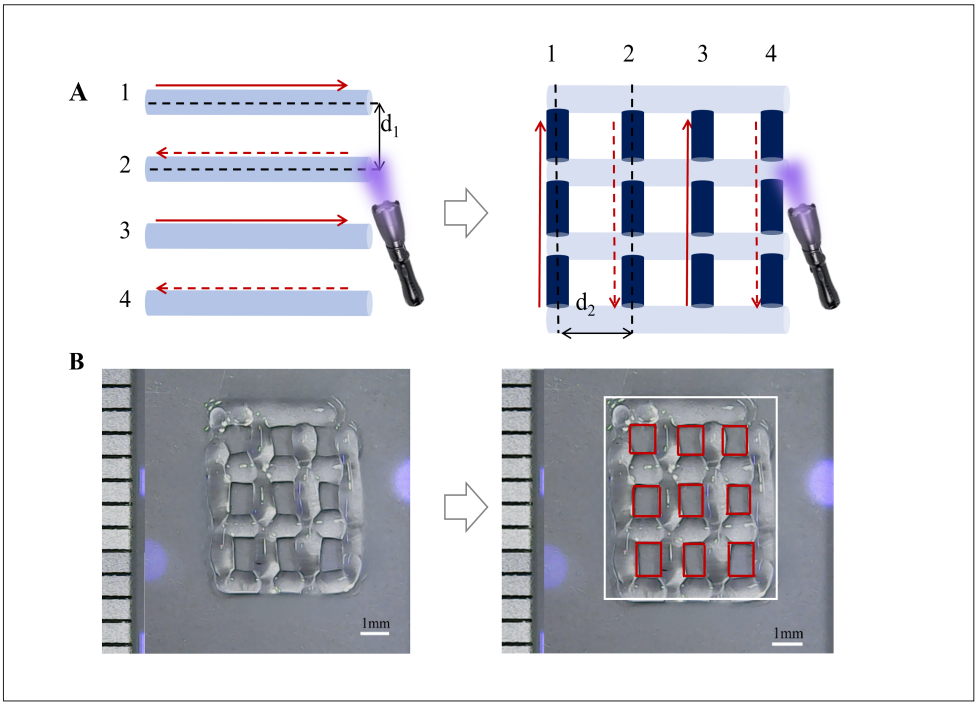

Figure 9. Schematic of improved printing path for (A) mesh scaffold and (B) photographs of the printed object.

Table 3. Dimensional statistic of sub-mesh across five experimental conditions

Experimental condition	Average length/width (mm)	CV of length/width (%)	Relative error (%)
1	1.18/1.10	1.94/1.87	2.41/−3.96
2	1.16/1.11	2.37/1.28	0.58/−3.09
3	1.11/1.12	1.58/1.41	−2.71/−2.61
4	1.15/1.11	2.29/1.69	0.19/−3.48
5	1.19/1.09	1.94/1.84	2.41/−5.51

Abbreviation: CV, coefficient of variation.

width and smoothness, establishing a direct correlation between input power and line width. This enables the controlled printing of lines with specific widths and smooth boundaries. Based on the developed printing parameter control method, mesh structures with individual unit dimensions of 1.15 × 1.15 mm were printed. The consistency of length and width across nine sub-meshes was evaluated by fitting a minimum bounding rectangle. The CVs for the lengths and widths of the nine sub-mesh units did not exceed 3%, and the relative errors between the measured and preset dimensions were less than 6%.

By integrating predictive droplet velocity control with optimized printing parameters, this work establishes a directly applicable parameter control strategy for acoustic droplet bioprinting. This strategy enables efficient selection of excitation and printing conditions, thereby improving printing efficiency while enhancing the fidelity and dimensional accuracy of printed structures. In addition, it provides a transferable methodological reference for extending acoustic droplet bioprinting to applications such as drug development, personalized medicine, and synthetic biology.

Acknowledgments

None.

Funding

This work is supported by the National Natural Science Foundation of China (No. 12304532) and the Natural Science Foundation of Tianjin (No. 23JCQNJC01320).

Conflict of interest

The authors declare no conflict of interest.

Author contributions

Conceptualization: Qing Guo, Dachao Li
Formal analysis: Qing Guo, Siyu Li
Investigation: Qing Guo, Siyu Li
Methodology: Qing Guo
Writing–original draft: Qing Guo
Writing–review & editing: Qing Guo, Dachao Li, Haixia Yu

Ethics approval and consent to participate

Not applicable.

Consent for publication

Not applicable.

Availability of data

Data are available from the corresponding author upon reasonable request.

References

1. Lechler RI, Sykes M, Thomson AW, Turka LA. Organ transplantation—how much of the promise has been realized? *Nat Med*. 2005;11(6):605-613.
doi: 10.1038/nm1251

2. Giwa S, Lewis JK, Alvarez L, *et al*. The promise of organ and tissue preservation to transform medicine. *Nat Biotechnol*. 2017;35(6):530-542.
doi: 10.1038/nbt.3889

3. Berthiaume F, Maguire TJ, Yarmush ML. Tissue engineering and regenerative medicine: history, progress, and challenges. *Annu Rev Chem Biomol Eng*. 2011;2(1):403-430.
doi: 10.1146/annurev-chembioeng-061010-114257

4. Van Blitterswijk C, De Boer J. Tissue Engineering. Cambridge, MA, USA: Academic Press; 2022.
doi: 10.1016/C2020-0-01481-7

5. Paxton N, Smolan W, Böck T, Melchels F, Groll J, Jungst T. Proposal to assess printability of bioinks for extrusion-based bioprinting and evaluation of rheological properties governing bioprintability. *Biofabrication*. 2017;9(4):044107.
doi: 10.1088/1758-5090/aa8dd

6. Ozbolat IT, Hospodiuk M. Current advances and future perspectives in extrusion-based bioprinting. *Biomaterials*. 2016;76(37):321-343.
doi: 10.1016/j.biomaterials.2015.10.076

7. Li X, Liu B, Pei B, *et al*. Inkjet bioprinting of biomaterials. *Chem Rev*. 2020;120(19):10793-10833.
doi: 10.1021/acs.chemrev.0c00008

8. Angelopoulos I, Allenby MC, Lim M, Zamorano M. Engineering inkjet bioprinting processes toward translational therapies. *Biotechnol Bioeng*. 2020;117(1):272-284.
doi: 10.1002/bit.27176

9. Guillotin B, Souquet A, Catros S, *et al*. Laser assisted bioprinting of engineered tissue with high cell density and microscale organization. *Biomaterials*. 2010;31(28):7250-7256.
doi: 10.1016/j.biomaterials.2010.05.055

10. Ventura RD. An overview of laser-assisted bioprinting (LAB) in tissue engineering applications. *Med Lasers Eng Basic Res Clin Appl*. 2021;10(2):76-81.
doi: 10.25289/ML.2021.10.2.76

11. Melchels FP, Feijen J, Grijpma DW. A review on stereolithography and its applications in biomedical engineering. *Biomaterials*. 2010;31(24):6121-6130.
doi: 10.1016/j.biomaterials.2010.04.050

12. Skoog SA, Goering PL, Narayan RJ. Stereolithography in tissue engineering. *J Mater Sci Mater Med*. 2014;25(3):845-856.
doi: 10.1007/s10856-013-5107-y

13. Murphy SV, Atala A. 3D bioprinting of tissues and organs. *Nat Biotechnol*. 2014;32(8):773-785.
doi: org/10.1038/nbt.2958

14. Krainer S, Smit C, Hirn U. The effect of viscosity and surface tension on inkjet printed picoliter dots. *RSC Adv*. 2019;9(54):31708-31719.
doi: 10.1039/c9ra04993b

15. Castro JO, Ramesan S, Rezk AR, Yeo LY. Continuous tuneable droplet ejection via pulsed surface acoustic wave jetting. *Soft Matter*. 2018;14(28):5721-5727.
doi: 10.1039/c7sm02534c

16. Guo Q, Su X, Zhang X, Shao M, Yu H, Li D. A review on acoustic droplet ejection technology and system. *Soft Matter*. 2021;17(11):3010-3021.
doi: 10.1039/d0sm02193h

17. Derakhshanfar S, Mbeleck R, Xu K, Zhang X, Zhong W, Xing M. 3D bioprinting for biomedical devices and tissue engineering: a review of recent trends and advances. *Bioact Mater*. 2018;3(2):144-156.
doi: 10.1016/j.bioactmat.2017.11.008

18. Hadimioglu B, Stearns R, Ellson R. Moving liquids with sound: the physics of acoustic droplet ejection for robust laboratory automation in life sciences. *J Lab Autom*. 2016;21(1):4-18.
doi: 10.1177/2211068215615096

19. Lagus TP, Edd JF. High-throughput co-encapsulation of self-ordered cell trains: cell pair interactions in microdroplets. *RSC Adv*. 2013;3(43):20512-20522.
doi: 10.1039/C3RA43624A

20. Jentsch S, Nasehi R, Kuckelkorn C, Gundert B, Aveic S, Fischer H. Multiscale 3D bioprinting by nozzle-free acoustic droplet ejection. *Small Methods*. 2021;5(6):2000971.
doi: 10.1002/smtd.202000971

21. Xia Y, Chen H, Li J, *et al*. Acoustic droplet-assisted superhydrophilic–superhydrophobic microarray platform for high-throughput screening of patient-derived tumor spheroids. *ACS Appl Mater Interfaces*. 2021;13(20):23489-23501. doi: 10.1021/acsami.1c06655

22. Chen K, Jiang E, Wei X, *et al*. The acoustic droplet printing of functional tumor microenvironments. *Lab Chip*. 2021;21(8):1604-1612. doi: 10.1039/d1lc00003a

23. Gong Z, Huang L, Tang X, *et al*. Acoustic droplet printing tumor organoids for modeling bladder tumor immune microenvironment within a week. *Adv Healthc Mater*. 2021;10(22):2101312. doi: 10.1002/adhm.202101312

24. Fang Y, Frampton JP, Raghavan S, *et al*. Rapid generation of multiplexed cell cocultures using acoustic droplet ejection followed by aqueous two-phase exclusion patterning. *Tissue Eng Part C Methods*. 2012;18(9):647-657. doi: 10.1089/ten.TEC.2011.0709

25. Guo Q, Shao M, Su X, Zhang X, Yu H, Li D. Controllable droplet ejection of multiple reagents through focused acoustic beams. *Langmuir*. 2021;37(51):14805-14812. doi: 10.1021/acs.langmuir.1c02450

26. Gudapati H, Dey M, Ozbolat I. A comprehensive review on droplet-based bioprinting: past, present and future. *Biomaterials*. 2016;102:20-42. doi: 10.1016/j.biomaterials.2016.06.012

27. Gong Y, Bi Z, Bian X, *et al*. Study on linear bio-structure print process based on alginate bio-ink in 3D bio-fabrication. *Bio Des Manuf*. 2020;3(2):109-121. doi: 10.1007/s42242-020-00065-9

28. Xiao S, Zhao T, Wang J, *et al*. Gelatin methacrylate (GelMA)-based hydrogels for cell transplantation: an effective strategy for tissue engineering. *Stem Cell Rev Rep*. 2019;15(5):664-679. doi: 10.1007/s12015-019-09893-4

29. Mamidi N, Ijadi F, Norahan MH. Leveraging the recent advancements in GelMA scaffolds for bone tissue engineering: an assessment of challenges and opportunities. *Biomacromolecules*. 2023;25(4):2075-2113. doi: 10.1021/acs.biomac.3c00279

30. Lemmo AV, Fisher JT, Geysen HM, Rose DJ. Characterization of an inkjet chemical microdispenser for combinatorial library synthesis. *Anal Chem*. 1997;69(4):543-551. doi: 10.1021/ac960808v

31. Gao H, Luo X, Cui D, *et al*. A study of film thickness and hydrodynamic entrance length in liquid laminar film flow along a vertical tube. *AIChE J*. 2018;64(6):2078-2088. doi: 10.1002/aic.16081

32. Ji Y, Yang QZ, Huang GY, *et al*. Improved resolution and fidelity of droplet-based bioprinting by upward ejection. *ACS Biomater Sci Eng*. 2019;5(8):4112-4121. doi: 10.1021/acsbiomaterials.9b00400

33. Qian J, Law CK. Regimes of coalescence and separation in droplet collision. *J Fluid Mech*. 1997;331:59-80. doi: 10.1017/S0022112096003722

34. Brazier-Smith P, Jennings S, Latham J. The interaction of falling water drops: coalescence. *Proc R Soc Lond A Math Phys Sci*. 1972;326(1566):393-408. doi: 10.1098/rspa.1972.0016

35. Cui Z, Feng Y, Liu F, Jiang L, Yue J. 3D bioprinting of living materials for structure-dependent production of hyaluronic acid. *ACS Macro Lett*. 2022;11(4):452-459. doi: 10.1021/acsmacrolett.2c00037